This is the submitted version of the article:

Ros C., Andreu T., David J., Arbiol J., Morante J.R..
Degradation and regeneration mechanisms of NiO protective layers deposited by ALD on photoanodes. Journal of Materials Chemistry A, (2019). 7. : 21892 - . 10.1039/c9ta08638b.

Available at: https://dx.doi.org/10.1039/c9ta08638b

About Degradation and Regeneration Mechanisms of NiO Protective Layers Deposited by ALD on Photoanodes

Carles Ros,[a,] Teresa Andreu,[a,b,*] Jérémy David,[c] Jordi Arbiol,[c,d] Joan R. Morante[a,b]*

[a] Catalonia Institute for Energy Research (IREC). Jardins de les Dones de Negre 1, 08930 Sant Adrià del Besòs, Barcelona, Spain

[b] Universitat de Barcelona (UB), Martí i Franquès, 1, 08028 Barcelona, Spain

[c]Catalan Institute of Nanoscience and Nanotechnology (ICN2), CSIC and The Barcelona Institute of Science and Technology (BIST), Campus UAB, Bellaterra, 08193 Barcelona, Spain

[d]ICREA, Pg. Lluís Companys 23, 08010 Barcelona, Spain

KEYWORDS

ALD, protective layers, water splitting, nickel oxide, regeneration, degradation

ABSTRACT

The use of high pH electrolytes requires protective layers to avoid corrosion in photoanodes based on semiconductors like silicon. NiO is one of the materials that complies the requirements of transparency, conductivity, chemical stability and catalysis on its surface in contact with the electrolyte. Here, these layers have been deposited by atomic layer deposition (ALD) at low temperatures, and their stability is analyzed over 1000 hours. Due to the layer structure characteristics, best overall performance has been achieved at 100 ºC deposition

temperature. By electrochemical measurements progressive time dependent degradation under anodic working conditions is observed, attributed to the formation of higher nickel oxidation states at the electrode/electrolyte interface as a main degradation mechanism, resulting in an OER overpotential increase. Another minor degradation mechanism affects the optical surface quality and gives rise to a loss of photon absorption efficiency in the hundreds of hours scale. A regeneration process based on an in situ periodic cyclic voltammetries, bringing the electrodes to cathodic conditions every 3, 12 or 48 hours, has shown to partially recover the main degradation mechanism achieving 85% of stability over 1000 hours in a study with over 10 $mA \cdot cm^{-2}$ photocurrent densities.

INTRODUCTION

As our society turns in the direction of a renewable based energy system, new challenges appear[1]. To store one of the most abundant energy sources, the sun, to be used when it is not available, photoelectrochemical (PEC) water splitting offers a clean and direct path[2–4]. The produced hydrogen can be either stored for further conversion into electricity with fuel cell technologies[5,6] or used in chemical process such as CO_2 revalorization[7] and other chemical products fabrication.

For many years metal oxides have been investigated and optimized, but efficiencies are limited and far from productivity requirements to industrialize this technique[4,8–11]. During the last decade significant efforts have been put into using already known efficient photovoltaic materials such as Si[12–14], InP[15,16], GaAs[17–19], CIGS/CZTS[20–24], but corrosion in highly acidic or alkaline electrolytes must be avoided. Covering the photoabsorbing materials with chemically resistant, electrically conductive, optically transparent and catalytic layers has given significant results, but there is still room to reduce degradation, device fabrication complexity, costs and adaptation to photoabsorber limitations[4,25–28].

TiO_2 has been the most used protective layer for photoanodes during last years, always combined with a catalyst layer or particles such as IrO_2, Pt, Ni, or Ni-Fe[19,26,29,30]. In a recent work[31], we have found the significant role played by the conduction mechanisms trough TiO_2 concerning the identified instability over long periods when in contact with alkaline environments at anodic oxidative potentials. The mechanisms related to the OH^- diffusion inside TiO_2 were analyzed, causing degradation in TiO_2 layers working under anodic conditions. The preferential conduction paths observed and attributed to grain boundaries and defects within the crystalline structure are altered in such conditions, changing the conductivity through the protective layer. Therefore, following these findings, there is still room for alternative materials which can assure better performance for very long-term under OER conditions.

In this study, we use NiO layers grown by atomic layer deposition (ALD) on silicon p-n junctions to efficiently fulfil all the required parameters as protective layers for PEC water splitting in alkaline environments (chemical resistance, photoabsorber protection, conductivity, transparency and catalytic effectivity for the oxygen evolution reaction (OER)) in a single step at low temperature fabrication process. NiO has a 3.8-4 eV band gap[32], with expected low visible spectra absorption coefficient. Moreover, it is also expected to be highly stable in alkaline media, forming nickel compounds in its surface, some of them more favorable for the OER water splitting reaction[33]. Likewise, NiO is known to have p-type semiconductor behavior[34], although some works report up to three orders of magnitude lower conductivity than titanium dioxide[35,36].

A standard silicon based frontal photoanode has been selected as supporting electrode for this study. ALD allows obtaining very conformal and pinhole-free layers, characteristics highly favorable for protective layers[37]. Low crystallization temperature is also a characteristic of

ALD[14,38], and is needed to avoid degradation of sensible photoabsorbers such as CIGS and CZTS as we demonstrated in other works[23,24].

In this work we report the degradation and regeneration mechanisms over 1000 hours anodic photocurrent of the NiO protected layers deposited at low temperature (100 ºC) in a single-step ALD deposition. Due to higher crystallinity and better stoichiometry as deposition temperature increases (100 to 300ºC), which is expected to reduce acceptors density, the higher electrical conductivity has been found at the lower temperature. Although, at this lowest temperature, the optical transmittance is smaller limiting also the layer capability.

On the other hand, NiO regeneration capabilities are shown with an in situ periodic cyclic voltammetry process, bringing the electrodes to cathodic conditions after anodic periods of different duration. Under these procedures, a partial recovery has been shown, achieving 85% of stability over 1000 hours. This opens a route for potential self-regeneration strategies of the catalyst/protective layers.

MATERIALS AND METHODS

ALD NiO has been grown on laboratory standard p^+n silicon buried junctions prepared as frontal photoanodes and simultaneously on p^+ degenerately doped silicon, to simulate direct injection in dark conditions.

p^+-Si samples were created by cutting a degenerately doped silicon wafer (0.001 ohm·cm) into 1x1 cm^2 pieces, and 50 nm Al were thermally evaporated as back contact.

p^+n-Si samples were fabricated as in previous works[14,31,39], where a 0.5 cm^2 active area was lithographically defined by SiO_2 passivation on a silicon n-type wafer (0.1-0.5 ohm·cm resistivity). Boron was implanted in the defined front surface and activated by rapid thermal annealing, creating a 200 nm p^+ region on top of the n-type substrate. As back contact, 1 µm Al/0.5%Cu was sputtered on top of 30 nm Ti to form a proper ohmic contact.

p^+-Si, and p^+n-Si samples were sonicated for 5 min in a 1:1:1 isopropanol, acetone and DI water cleaning solution, followed by abundant rinsing and further 5 min sonication in DI water. Before ALD deposition, sample's front surface was dipped in 0.1 M HF for 5 min, rinsed in DI water and immediately introduced in the ALD chamber.

A Cambridge Savannah 100 Atomic Layer Deposition system was used to grow NiO layers. $NiCp_2$ (nickelocene, bis(cyclopentadienyl)nickel) was selected as precursor and ozone (O_3) as reactant[40,41]. $NiCp_2$ container was heated at 80 ºC during the process. Successive pulses in N_2 flow atmosphere were introduced to the chamber, 4 s pulses, 10 s maintained in the chamber ("expo" mode) and 20 s purges for $NiCp_2$, and 20 s pulse and 40 s purge for O_3. Under these conditions, layers have been grown at deposition temperatures of 100, 200 and 300 ºC for 1000 cycles, corresponding to roughly 50 nm layers, too thick for real protective layers but robust enough for manipulation during the degradation experiments. Samples were then soldered to a Cu wire using Ag paint and epoxy protected leaving the front area exposed (Fig. S. 1).

Surface morphology and cross section were observed with a Zeiss Series Auriga Field Effect Scanning Electron Microscope (FESEM). Structural characterization was carried out by X-ray diffraction (XRD) in a D8 Advance Bruker equipment with a Cu Kα radiation source working at 40 kV and 40 mA with a 1 º offset angle. Crystalline domains are calculated following the Scherrer equation: $D = 0.9 * \lambda / (\beta * \cos\theta)$, where λ is the X-ray wavelength (1.5406 Å), β is the full width of the diffraction line at half maximum (FWHM), and θ is the Bragg angle. High resolution transmission electron microscopy (HRTEM) was performed using a TECNAI F20 operated at 200 kV with a point to point resolution of 0.14 nm. AFM and conductivity AFM (c-AFM) measures were taken with a Park Systems XE-100 with platinum conductive cantilevers and biasing the sample at +1.5 V respect to the tip. Due to the p^+n-Si built-in voltage, only the samples on p^+-Si substrates were measured by c-AFM. The photoelectrochemical measurements were obtained with a Biologic VMP-300 potentiostat

using Ag/AgCl/KCl(sat) (E^0 = 0.197 V_{RHE}) as reference electrode and platinum mesh as counter electrode. A quartz cell with flat faces was used with 100 ml of 1 M KOH electrolyte and a 300 W xenon lamp with an AM 1.5G filter under the appropriate distance to receive 100 mW/cm^2, calibrated using a silicon diode (Gentec-EO, XLPF12-3S-H2-DO). Electrochemical impedance spectroscopy was obtained with 25 mV amplitude and scanning from 100 kHz to 1 Hz. I-V curves were obtained depositing 50 nm of Ni on the front surface of the samples and measuring with the potentiostat in four points probe configuration, connecting two at the back contact and the other two at the top Ni contact.

RESULTS AND DISCUSSION

Photoelectrochemical, Electrical and Morphological Characterization

NiO layers grown by ALD were fabricated at 100, 200 and 300 ºC deposition temperatures on top of p^+n-Si, p^+-Si, FTO and glass. This range was selected to investigate low deposition temperatures, as some photoabsorbers require avoiding high temperatures in order to prevent any alteration[23,24]. In Fig. 1 we present representative cyclic voltammograms of the first 100 cycles measured for these samples. In dark conditions, measurements were performed using layers deposited on top of p^+ silicon anodes, and, under 1 sun simulated illumination, using layers deposited on top of p^+n-Si junctions. A clear dependence can be seen in both cases, with significantly higher currents when depositing at 100 ºC than at 200 ºC, further reduced when increasing to 300 ºC. Clear Ni^{2+}/Ni^{3+} peaks can be seen more cathodic than the OER onset potential, corresponding to Ni active sites[33,42,43] presenting steady increase with cycling. Slight activation is observed for the OER in the 1.8-1.9 V vs RHE range too. Both Ni peaks increase and initial activation are known to be caused by slight surface reorganization and residual Fe

ion traces incorporated from electrolyte impurities, being beneficial for efficient OER[42]. Transmittance on top of glass substrates was measured to be in the range of 40 to 80% (Fig. S. 2), reduced with lower deposition temperatures[36]. NiO is known to be less transparent when increasingly defective [36,44,45]. This is expected to be directly translated into reduced maximum saturation photocurrent for photoanodes under illumination.

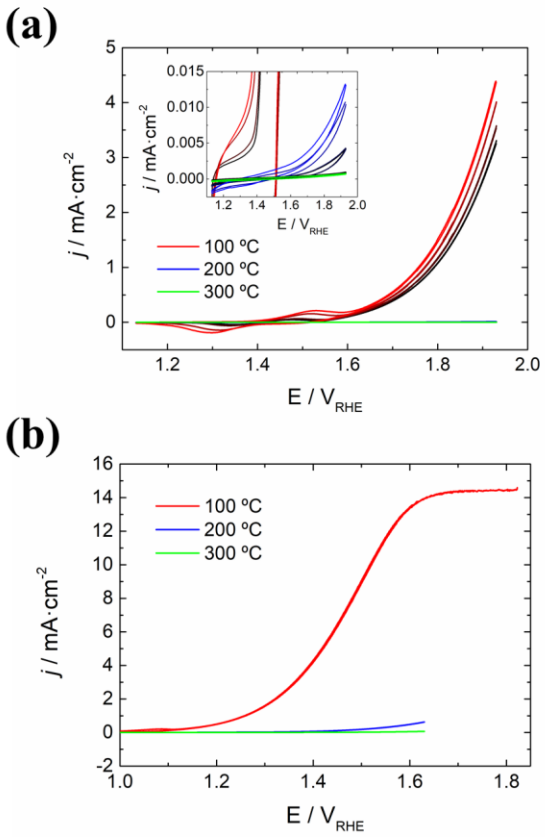

Fig. 1: cyclic voltammograms in 1 M KOH of a) p^+-Si anodes protected with ALD deposited NiO layers at 100 ºC (red) 200 ºC (blue) and 300 ºC (green), cycles 1, 10, 50 and 100 from darker to clearer color. Zoom in the 200 and 300 ºC is presented in the inset. b) p^+n-Si photoanodes under 1 sun illumination.

To exclude any influence of the electrolyte contact, Ni metallic contacts were deposited on top of p^+-Si devices and I-V measurements were also carried out. In Fig. 2 it can clearly be seen conductivity to depend on deposition temperature as it has been seen in Fig. 1. Likewise, 100 ºC deposited layers are significantly more resistive than the p^+-Si/Ni contact with a rectifying behavior.

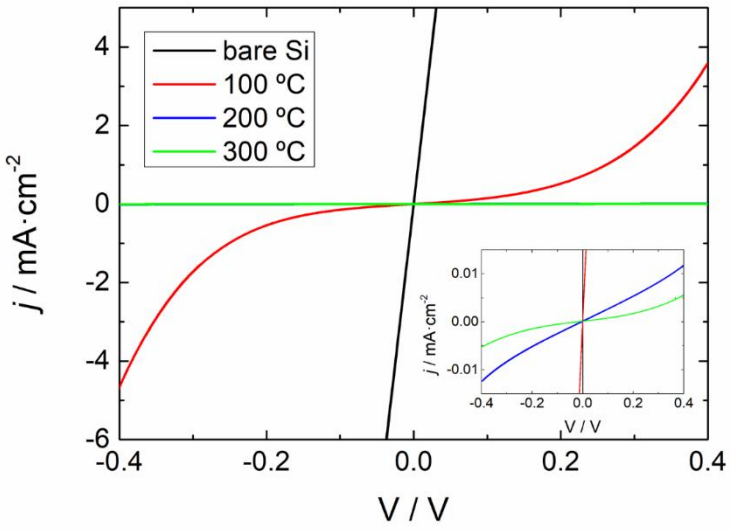

Fig. 2: I-V measurements of NiO layers grown on p^+-Si at ALD deposition temperatures of 100, 200 and 300 ºC and further 50 nm Ni deposited as top contact. A sample with Ni directly deposited on top of p^+-Si is considered as reference.

From SEM analysis (Fig. 3, a-c), we do not observe any significant differences upon deposition temperature. Samples present complete surface coverage, with a measurable thickness by cross section of around 50 nm, as predicted (Fig. 4). A granular rugose surface is observed for all deposition temperatures in the range of ~20 nm, close to the resolution limit of the SEM, slightly more pronounced for 300 ºC deposition temperature. Main differences are deduced from the XRD spectra. Bunsenite crystallographic structure is measured for all the deposition temperatures, but major orientation changes happen when increasing it. At 100 ºC a single

exposed crystallographic facet is measured, with a diffraction angle of 37.37 º associated to the 111 direction. On the contrary, for the 200 and 300 ºC deposition temperatures, a preferential peak of 43.48 º is measured. Crystalline interplanar spacing (*d*) was measured to be reduced at higher temperatures, together with the full width at half maximum (β, FWHM). Using the Scherrer equation, crystalline domains (*D*) are measured to be 18.8, 14.7 and 24.1 nm for 100, 200 and 300 ºC. All this is information is resumed in Table 1. The variation with temperature are difficult to analyze, as there is a simultaneous change in the dominant orientation from 111 to 200. These trends are coherent with the results found for the sputter-deposited NiO films, which nucleate and grow preferentially in the (111) plane direction at room temperature if sufficient oxygen is available, whereas they show a (200) crystal orientation if deposition temperature is increased [46–48]. The slight shift to higher diffraction angles from 200 to 300 ºC can he attributed to compressive stress or to more stoichiometric NiO, reducing the cell volume (interplanar spacing, *d*)[49].

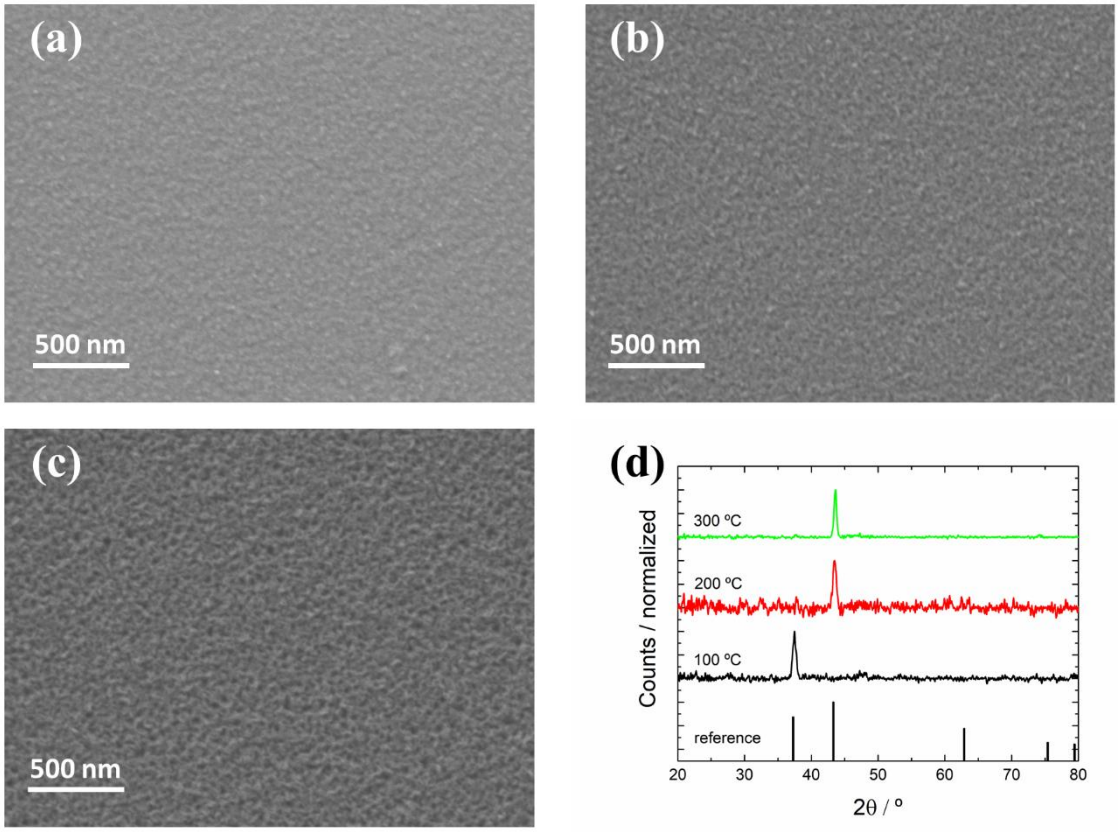

Fig. 3: SEM images of NiO films grown on top of Si at a) 100 b) 200 and c) 300 ºC. d) XRD patterns of NiO films grown at different temperatures, compared to reference data JCPDS 00-047-1049.

Sample	**Preferential peak**	**2θ (º)**	**β, FWHM (º)**	***d* (Å)**	***D* (nm)**
Ref	1 1 1	37.249	-	2.412	-
Ref	2 0 0	43.276	-	2.089	-
100 ºC	1 1 1	37.37	0.5314	2.40639	18.8
200 ºC	2 0 0	43.48	0.7439	2.08135	14.7
300 ºC	2 0 0	43.61	0.4536	2.07364	24.1

Table 1: XRD measurements of NiO layers grown at 100, 200 and 300 ºC and compared to reference data from bunsenite NiO, corresponding to JCPDS 00-047-1049. Crystal orientation change can be observed between 100 and 200 ºC.

HRTEM of NiO layers grown at 100 ºC and 200 ºC (Fig. 4) present polycrystalline layers matching the bunsenite structure, with observed crystals being 10-20 nm, in the same range as crystalline domain (*D*) measured by XRD. FFT filtered images show crystals longer in vertical growth direction than horizontal, some of them propagating from substrate to surface.

Likewise, the HRTEM analysis reveals the existence of an unwanted SiO_x layer of about 5 nm thick, independent of deposition temperature. This parasitic layer is expected to introduce an extra tunnelling resistance to the system[50], and is attributed to the use of ozone, oxidizing the Si substrate during the first stages of the ALD deposition[51], as it is known to be an aggressive oxidant[52,53]. Although it should be avoided in order to improve the overall protected photoanode performances, it does not prevent the endurance analysis of these layers.

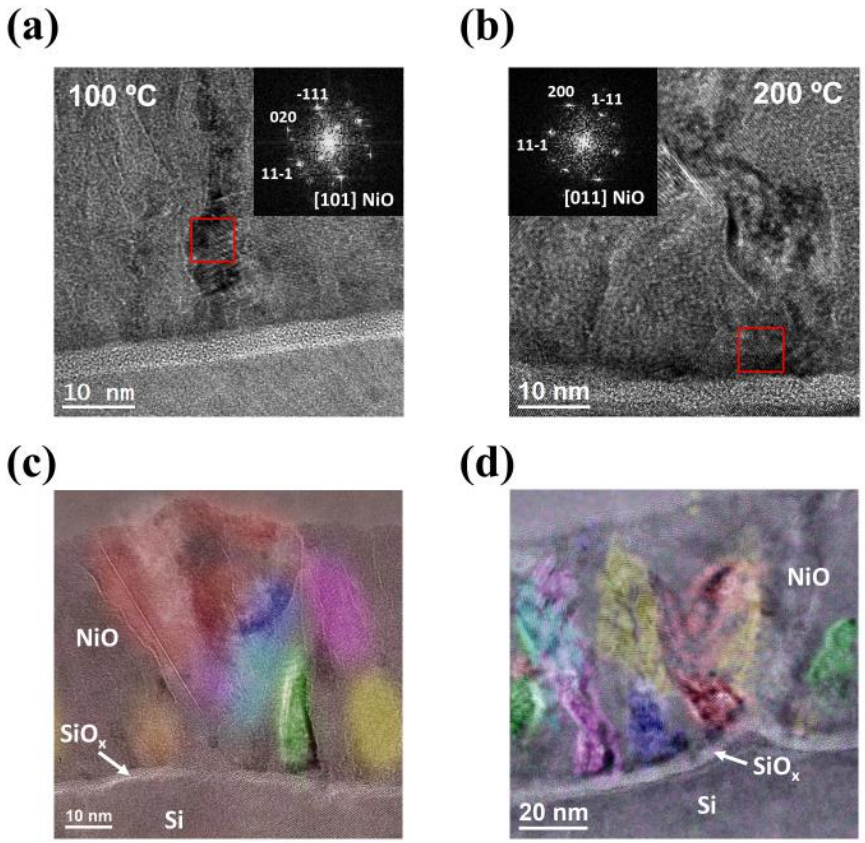

Fig. 4: HRTEM images of NiO films grown on Si at 100 (a and c) and 200 ºC (b and d). A SiO_x thin layer of ~ 5 nm can be observed, not modified with temperature. NiO crystalline regions with the same crystallographic orientation have been colored with the same color, and can be observed in colored FFT structural filtered HRTEM, few of them being columnar from base to top. Non-flat surface of Si chips is caused by successive etching steps from masked p-n junction formation and isolation process.

Current mapping was measured by AFM. Again, lower conductivity is determined as deposition temperature is increased, following the same tendency as for cyclic voltammograms (Fig. 1) and I-V measurements (Fig. 2). Regions between grains present no conductivity, less observed when increasing deposition temperature, probably by a better crystallization (such as it has been determined by XRD). For 100 ºC, all grains appear as conductive, with a +/- 30% current dispersion. For 200 and 300 ºC, smaller grains are the ones appearing to be more

conductive, although overall conductivity is lower compared to 100 ºC (observe the different current scale). NiO is known to present oxygen anions migration under applied potentials[54], up to filament formation[55], although is not observed in our potential range.

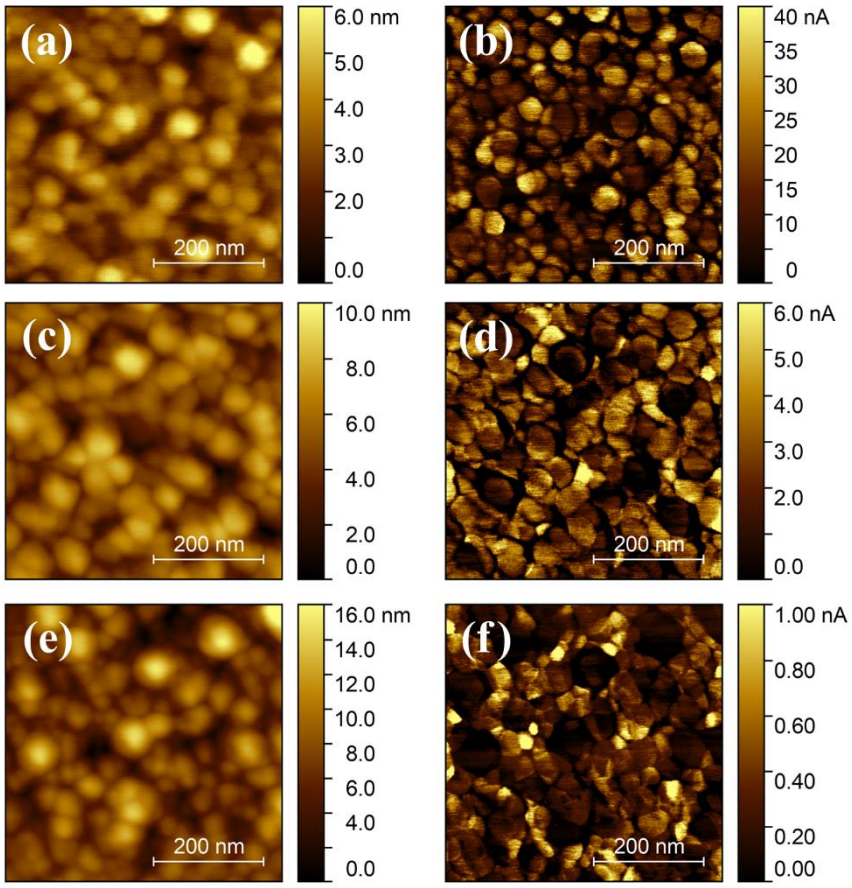

Fig. 5: Topography (a, c, e) and current (b, d, f) AFM images of NiO layers grown at 100 (a, b), 200(c, d) and 300 ºC (e, f). Grain size and distribution is not observed to vary, but rugosity increases with deposition temperature. Overall conductivity is reduced when deposition temperature is increased, with some crystals more conductive than others and grain boundaries observed as not conductive. Measurements performed biasing the sample at +1.5 V respect to the tip.

Gathering all these results, we find a relation between the deposition temperature, the crystal orientation and the conductivity, determining the overall benefit in using 100 ºC deposited layers. As can be seen in Fig. 3d, increasing deposition temperature in ALD changes the

preferential growth direction too. Higher deposition temperature gives more thermal energy, allowing the adsorbed atoms to diffuse longer distances and minimize surface energy to form more thermodynamically stable crystal structures, shifting from (111) XRD preferential plane orientation to the (200) one, improving crystallinity (Fig. 3d). This is expected to reduce point defects such as cationic Ni^{2+} vacancies, which were being compensated by neighboring atoms in Ni^{3+} states[52,56–58] acting as acceptors. Changes in these favorable imperfections due to atomic reorganization caused by temperature treatments or different layer growth process are crucial in achieving a conductive layer[36,52]. This diminishment on Ni^{2+} vacancies with increasing deposition temperature reduces NiO available acceptor levels, which are the majority charge carriers in p-type semiconductors, thus reducing film conductivity[36,46–48,59].

Scheme 1 describes a band structure where the photogenerated holes are injected into the NiO valence band through the tunnel barrier introduced by the parasitic SiO_2 layer. These injected holes must travel to the NiO/electrolyte interface overcoming the internal voltage loses caused by the low NiO layer conductivity.

When immersed in alkaline electrolytes and at anodic potentials, the NiO surface reacts with OH^- to form $Ni(OH)_2$ and NiOOH, known to modify the OER catalyst performance of the NiO surface[60–64]. With the valence band maximum located below the water oxidation level, there is no resistance expected as NiO surface has an accumulation zone in contact with the catalytic region[59].

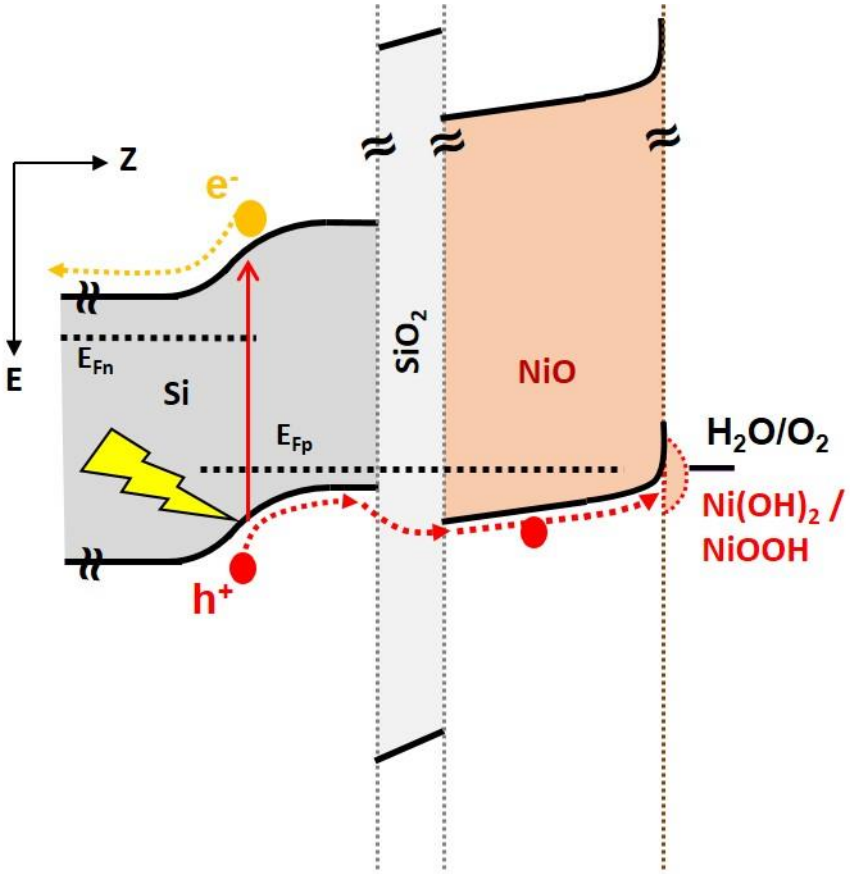

Scheme 1: Energy band diagram of a p^+n-Si photoanode, with the O_3-caused SiO_2 layer and ALD-NiO protected and with $Ni(OH)_2$/NiOOH as OER catalyst.

Electrochemical and Photoelectrochemical Stability Characterization.

100 ºC sample was analyzed by electrochemical impedance spectroscopy (EIS), and two semicircles were observed (Fig. 6a and Table S. 1). The one at high frequencies (left) is attributed to a depletion barrier in NiO film in its internal interface and the one at low frequencies (right) to OER catalysis. This one is drastically reduced at potentials more anodic than OER (~1.6 V vs RHE). Comparing with the EIS of a Ni foil in the same conditions, a single semicircle is observed for the metallic foil, with similar R and C values (at similar

current) to the low frequency arc of NiO, confirming it can be attributed to OER catalysis (Fig. S. 3 and Table S. 2).

100 ºC sample was left 24 h in stability at 1.9 V vs RHE (Fig. 6b) and anodic current decay was observed from 3 towards 2 $mA \cdot cm^{-2}$ during first hours. This decay points toward a logarithmic dependence[65] of current on time (Fig. S. 4), and could suggest the formation of a self-passivation layer and its corresponding introduced charge transfer resistance, lowering the current. The increase in resistance is also observed in periodical EIS (Fig. 6c and Table S. 3). Due to the temperature fluctuations in the laboratory affecting reaction kinetics, some variations are observed on the general current trend.

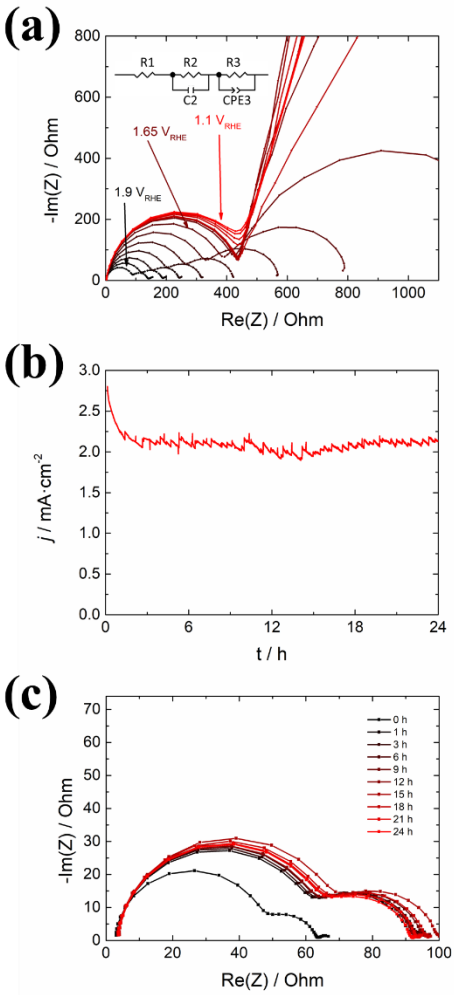

Fig. 6: a) EIS measurements at potentials from 1.1 to 1.9 V vs RHE in 1 M KOH of an ALD protected p^+-Si with 100 ºC NiO. The fitted circuit is represented in the inset. Obtained fitted values are presented in Table S. 1. b) 24 h stability measurement of the same sample at 1.9 V vs RHE in 1 M KOH. c) Periodical EIS measurements at 1.9 V vs RHE corroborating non-significant changes after initial decay. Obtained fitted values are presented in Table S. 3.

Thus, SEM images of 100 ºC sample revealed the presence of ~200 nm bumps formed on the surface after electrochemical testing (Fig. 7a and b), which were confirmed by EDX to be elementally composed of Ni and O (Fig. S. 5 and Table S. 4). 200 and 300 ºC ones presents no observable morphological changes (Fig. S. 6) after cycling (Fig. 1a) together with no significant measured current. These rounded porous structures are known to be characteristic of $Ni(OH)_2$ [66–68]. Cross section SEM revealed the NiO film does not show any evidence of significant variation of initially deposited ~50 nm.

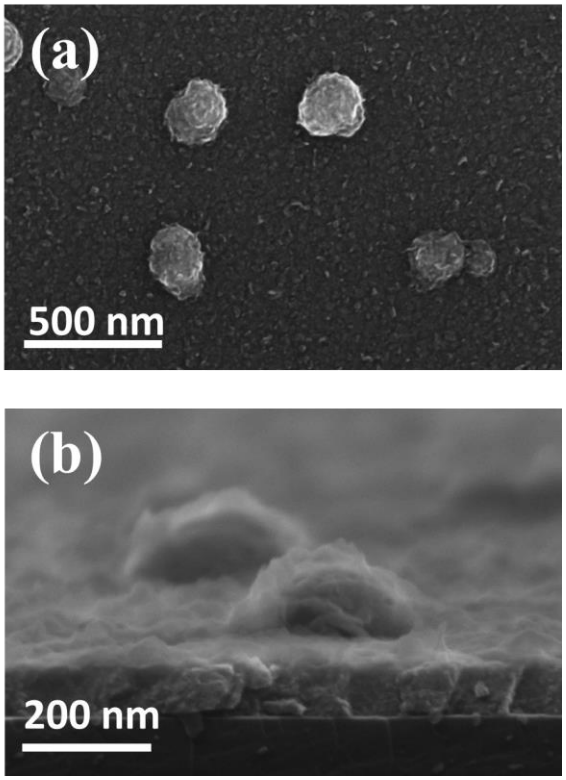

Fig. 7: a) SEM images of a NiO layer grown at 100 ºC on top of a p^+-Si anode in 1 M KOH after finishing the stability measurement and b) cross section.

Stability measurements were performed using a p^+n-Si photoanode, protected by a 100 ºC grown NiO layer (Fig. 8). Sample was polarized to 1.7 V vs RHE, the lowest potential to be considered in current saturation regime (where the current density is limited by the number of electron-hole pairs photogenerated in the p-n junction). Initially, this photoanode was cycled 6 times (voltage inversion from anodic to cathodic conditions) in 12 h intervals under 1 sun AM 1.5G illumination. After 500 h, the cycling period was increased to 48 h. Under these conditions, a higher current density decay can be observed from 12 to 9 $mA \cdot cm^{-2}$. If the cycling is reset to 12 h, the photocurrent recovers up to 11 $mA \cdot cm^{-2}$, and further reducing it to 3 h gives a slightly extra photocurrent reaching almost 12 $mA \cdot cm^{-2}$ at 1.7 V vs RHE (Fig. 8a,b). This test measurement was performed during 1000 h, where we stopped the experiment to be capable to further characterize the sample.

A photocurrent density constant decay of ~2 $mA \cdot cm^{-2}$ after 1000 h at 1.7 V vs RHE was observed. In Fig. S. 7 it is compared the current density during stability measurement at 1.7 V vs RHE with the slope at 8 $mA \cdot cm^{-2}$ (determined during the cyclic voltammograms) and current density values at the saturation potentials (1.8 V vs RHE). Also, some small fluctuations are visible (especially in Fig. 8b) due to lab night and day temperature variations.

These results reveal the more frequent application of cyclic voltammograms allows increased partial recovery of the passivation layer, and density current values are recovered.

Worthy information about these degradation and regeneration mechanisms can be deduced from a detailed analysis of the cyclic voltammograms measured during the 1000 h stability test (Fig. 8, c and d), presenting several remarkable characteristics.

First, an increase of the Ni^{2+}/Ni^{3+} redox peaks, which suggests a progressive increase of the nickel involved in the reaction, related bumps and flakes formed as observed comparing Fig. 3a and Fig. 7.

Second, a decrease of the electrochemical activity giving by a lowering of the slope in the 1.4-1.8 V vs RHE range. The detected self-passivation formed layer (previously mentioned) causes the lower slope, and points out an increase of the electrochemical overpotential due to the modification of the $Ni(OH)_2$/NiOOH catalytic surface. Minor internal voltage losses introduced by the self-passivation layer formed in the outermost layers of the NiO film are also possible. In Fig. S. 7 it is revealed how this mechanism governs photoanode's performance main decrease.

Third, a decrease of the saturation current, which must be attributed to a decrease of the amount of light reaching the photodiode. This is observed in Fig. S. 7 as a stable constant decay of the photocurrent measured for the performed periodic cyclic voltammograms until more anodic potentials than the stability potential.

It has been previously reported for NiO the existence of electrochromic darkening caused by surface ion adsorption[47] or electrochemical formation of less transparent NiOOH, with more Ni^{3+} in the surface, having lower optical band gap and higher absorption coefficient than NiO and $Ni(OH)_2$ [45]. Bumps and nanoflakes formation observed in Fig. 7 and related to the electrochemical modifications measured are plausible causes of absorption and scattering causing the transparency variation over 1000 h.

Resuming, in Fig. 8c and d one can observe the effects of two different degradation mechanisms. On one hand, there is the progressive variation of the slope, a self-passivation mechanism (observed in Fig. 6b too). This points out an increase of the electrochemical overpotential. It is noteworthy to mention simultaneous resistive losses in the outermost layers

of the NiO film is plausible. On the other hand, a steady decrease of the current density value in the current saturation potentials, which as we show below, is associated to the photon absorption efficiency due to a loss of the optical quality of the ALD-NiO surface.

So, NiO working in anodic conditions under alkaline electrolytes presents surface reorganization into $Ni(OH)_2$/NiOOH as measured in cyclic voltammetries and observed by SEM, with presented characteristic bumps and nanoflakes. Besides, comparing with the electrode potential−pH (Pourbaix) phase map diagram of NiO in aqueous electrolytes[69], our anodic applied potentials are close to the NiO_2 region, where nickel oxyhydroxides (most favorable phase to OER catalysis) is no more the principal nickel phase.

Thus, the two degradation mechanisms are attributed one to the effects on the electrochemical efficiency and another to the effects on the optical efficiency. Whereas this last process seems not reversible, the first one presents the advantage of the electrochemical reversibility. This is obtained by periodic cathodic polarizations as shown in Fig. 8c and d and the recovery is observed in the improved slopes of the cyclic voltammetries. Polarizing to potentials more cathodic than the Ni^{2+}/Ni^{3+} redox peak reduces back a significant portion of the previously mentioned unfavorable oxidized Ni states formed on the outermost nanometers of the NiO protective layer during the stability test.

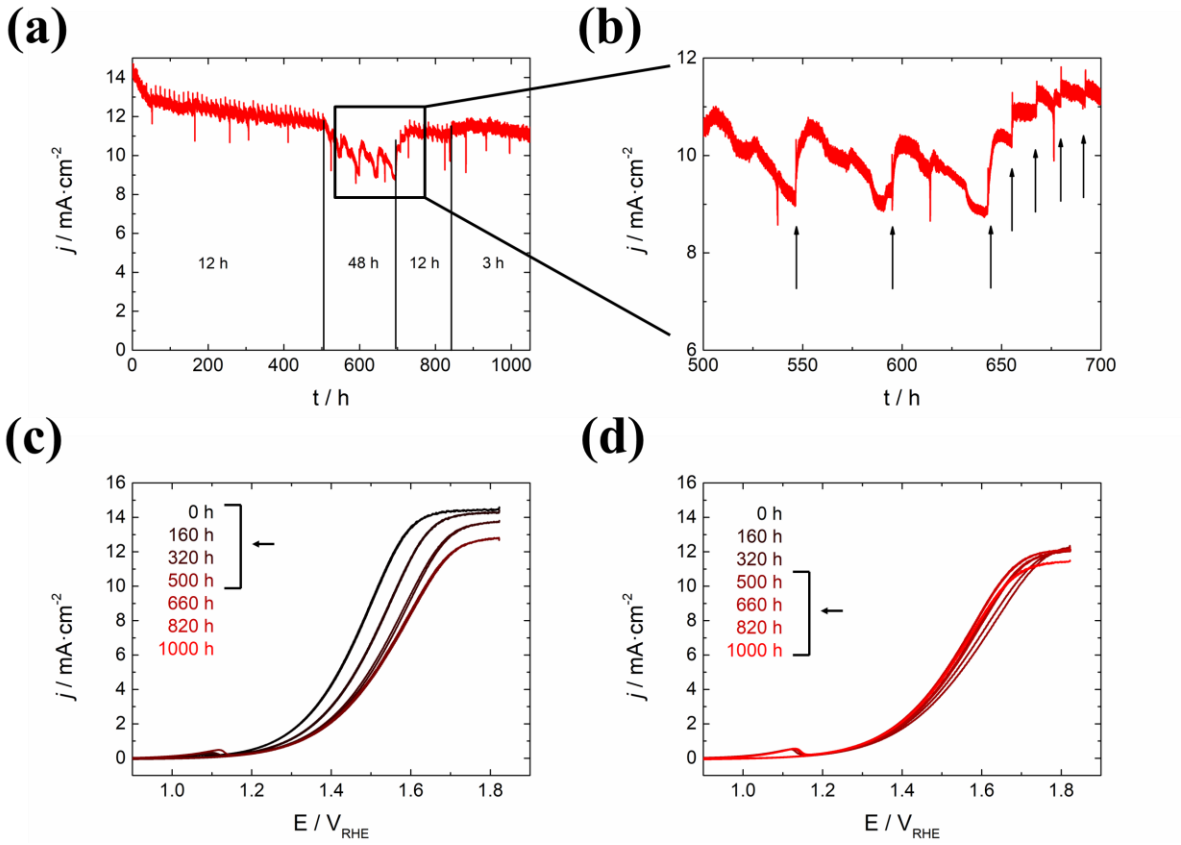

Fig. 8: p⁺n-Si photoanode protected with NiO deposited at 100 ºC and measured under 1 sun illumination in 1 M KOH. a) 1000 h stability measurement at 1.7 V vs RHE cycled 6 times every 12, 48 or 3h as indicated. b) Zoom of the region cycled every 48 h and 12 h, corresponding to the arrows. c) Cyclic voltammograms measured during first 500 h of the stability test, showing saturation current decrease and small hysteresis increase. d) Cyclic voltammograms starting on the last 48 h interval, where the sample was most degraded, and further recovered by smaller cycling intervals.

Finally, as complementary information, it can be observed that the SEM analysis presents few spots where the silicon beneath had been etched after 1000 h stability tests (5 in a 1 mm^2 area, a very low density, as observed in Fig. S. 8a-c). Analyzing them closely, we can see the protective layer is still present, and the alkaline electrolyte found a path in few specific spots

to reach the silicon etching it. On these few spots, in one case a particle was present and in the other one a hole, both of them exactly in the center. So, these pinholes in the protective layer are attributed to extrinsic or unwanted fabrication defects and not to intrinsic instability of the protection film, and thus, should be eliminated with optimal fabrication.

CONCLUSIONS

NiO transparent, protective, conductive and catalytic films grown by ALD have been used to avoid corrosion on frontal illuminated silicon photoanodes in alkaline electrolytes and anodic potentials while performing the oxygen evolution reaction.

Layers grown at 100, 200 and 300 ºC with thicknesses in the range of 50 nm present a polycrystalline structure with a change in preferential orientation when increasing from 100 ºC to 200 and 300 ºC, correlated with conductivity diminishment and transparency slight increase. The sample grown at 100ºC presents the best electrical conductivity and optical transparency compromise.

Stability measurements on best-performing 100 ºC NiO-protected photoanodes present degradation mechanisms. Current density decays following a logarithmic time dependency, pointing at the formation of a self-passivation layer, limiting the electrochemical efficiency. This is attributed to the interaction of the NiO layer and the alkaline electrolyte under anodic working conditions, forming of higher nickel oxidation states at the electrode/electrolyte interface, resulting in an OER overpotential increase. Under illumination, a second degradation mechanism is identified. A steady decrease of the current density at the current saturation potentials region is observed, attributed to losses of optical efficiency.

In the case of the electrochemical efficiency degradation, the application of periodic cycling ranging from anodic to cathodic voltage conditions corroborates the existence of a partial

recovery procedure. Likely, these cathodic scans promote reduced forms at the surface of the ALD NiO layer, reversing some oxidation processes occurring at anodic potentials in highly alkaline media.

Applying this methodology under 3 hours cycling periodicity, over 1000 h stability measurements were possible with over 10 $mA \cdot cm^{-2}$ photocurrents, an 85% of the initial photocurrent.

The few corrosion spots observed have been correlated to extrinsic origin and thus, NiO ALD was demonstrated as a successful technique for long-lasting protective layers in anodic and alkaline conditions, avoiding corrosion of Si photoelectrodes or other alternative semiconductors. Furthermore, the use of low deposition temperature (100 ºC) for NiO deposition would allow for temperature-sensitive photoabsorbers to be implemented in PEC anodic conditions.

Consequently, this procedure opens a promising strategy for driving stability in photoelectrochemical devices. This regenerative protocol switching to cathodic potentials represents less than 1% of the working time under anodic conditions. However, there is still room to fully understand regenerative pathway's and to enable very long stability, and thus should be studied also in other materials suffering from electrochemical degradation.

ASSOCIATED CONTENT

Supporting Information. Transmittance, EIS, SEM, and EDX supporting images, together with a photo of a finished device, are supplied in an additional document.

AUTHOR INFORMATION

Corresponding Author

*Corresponding authors:

E-mail: cros@irec.cat

E-mail: tandreu@irec.cat

Tel: (34) 933 562 615

Author Contributions

The manuscript was written through contributions of all authors. All authors have given approval to the final version of the manuscript.

Funding Sources

ACKNOWLEDGMENT

Authors from IREC acknowledge Generalitat de Catalunya for financial support through the CERCA Programme, M2E (2014SGR1638). IREC also acknowledges additional support by the European Regional Development Funds (ERDF, FEDER) and by MINECO coordinated projects MAT2014-59961-C2, ENE2016-80788-C5-5-R and ENE2017-85087-C3. C.R. acknowledges MINECO for his FPI grant (BES-2015-071618). ICN2 was supported by the Severo Ochoa program from Spanish MINECO (Grant No. SEV-2017-0706) and was funded by the CERCA Programme/Generalitat de Catalunya. ICN2 acknowledge funding from Generalitat de Catalunya 2017 SGR 327 and the Spanish MINECO project ENE2017-85087-C3. J.D. received funding from the European Union's Horizon 2020 research and innovation programme under the Marie Sklodowska-Curie grant agreement No. 665919 (P-SPHERE) co-funded by Severo Ochoa Programme.

REFERENCES

(1) Lewis, N. S.; Nocera, D. G. Powering the Planet: Chemical Challenges in Solar Energy Utilization. *Proc. Natl. Acad. Sci. U. S. A.* **2006**, *103* (43), 15729–15735.

(2) Tuller, H. L. Solar to Fuels Conversion Technologies: A Perspective. *Mater. Renew. Sustain. Energy* **2017**, *6* (1), 1–16.

(3) James, B. D.; Baum, G. N.; Perez, J.; Baum, K. N. Technoeconomic Analysis of Photoelectrochemical (PEC) Hydrogen Production. **2009**, 1–128.

(4) Lewis, N. S. Developing a Scalable Artificial Photosynthesis Technology through Nanomaterials by Design. *Nat. Nanotechnol.* **2016**, *11* (12), 1010–1019.

(5) Berry, G. D.; Pasternak, A. D.; Rambach, G. D.; Smith, J. R.; Schock, R. N. Hydrogen as a Future Transportation Fuel. *Energy* **1996**, *21* (4), 289–303.

(6) Wang, M. Fuel Choices for Fuel-Cell Vehicles: Well-to-Wheels Energy and Emission Impacts. *J. Power Sources* **2002**, *112* (1), 307–321.

(7) Yao, Y.; Liu, X.; Hildebrandt, D.; Glasser, D. Fischer–Tropsch Synthesis Using H_2 /CO/CO_2 Syngas Mixtures over an Iron Catalyst. *Ind. Eng. Chem. Res.* **2011**, *50* (19), 11002–11012.

(8) Fujishima, A.; Honda, K. Electrochemical Photolysis of Water at a Semiconductor Electrode. *Nature* **1972**, *238* (5358), 37–38.

(9) Rahimi, N.; Pax, R. A.; Gray, E. M. A. Review of Functional Titanium Oxides. I: TiO2 and Its Modifications. *Prog. Solid State Chem.* **2016**, *44* (3), 86–105.

(10) Tang, P.; Xie, H.; Ros, C.; Han, L.; Biset-Peiró, M.; He, Y.; Kramer, W.; Rodríguez, A. P.; Saucedo, E.; Galán-Mascarós, J. R.; et al. Enhanced Photoelectrochemical Water Splitting of Hematite Multilayer Nanowire Photoanodes by Tuning the Surface

State via Bottom-up Interfacial Engineering. *Energy Environ. Sci.* **2017**, *10* (10), 2124–2136.

(11) Ros, C.; Fabrega, C.; Monllor-Satoca, D.; Hernández-Alonso, M. D.; Penelas-Pérez, G.; Morante, J. R.; Andreu, T. Hydrogenation and Structuration of TiO 2 Nanorods Photoanodes: Doping Level and the Effect of Illumination in Trap-States Filling. *J. Phys. Chem. C* **2018**, *122* (6), 3295–3304.

(12) Xia, Z.; Zhou, X.; Li, J.; Qu, Y. Protection Strategy for Improved Catalytic Stability of Silicon Photoanodes for Water Oxidation. *Sci. Bull.* **2015**, *60* (16), 1395–1402.

(13) Sun, K.; Shen, S.; Liang, Y.; Burrows, P. E.; Mao, S. S.; Wang, D. Enabling Silicon for Solar-Fuel Production. *Chem. Rev.* **2014**, *114* (17), 8662–8719.

(14) Ros, C.; Andreu, T.; Hernández-Alonso, M. D.; Penelas-Pérez, G.; Arbiol, J.; Morante, J. R. Charge Transfer Characterization of ALD-Grown TiO2 Protective Layers in Silicon Photocathodes. *ACS Appl. Mater. Interfaces* **2017**, *9* (21), 17932–17941.

(15) Lee, M. H.; Takei, K.; Zhang, J.; Kapadia, R.; Zheng, M.; Chen, Y.-Z.; Nah, J.; Matthews, T. S.; Chueh, Y.-L.; Ager, J. W.; et al. P-Type InP Nanopillar Photocathodes for Efficient Solar-Driven Hydrogen Production. *Angew. Chemie Int. Ed.* **2012**, *51* (43), 10760–10764.

(16) Wang, T.; Gong, J. Single-Crystal Semiconductors with Narrow Band Gaps for Solar Water Splitting. *Angew. Chemie - Int. Ed.* **2015**, *54* (37), 10718–10732.

(17) Licht, S.; Wang, B.; Mukerji, S.; Soga, T.; Umeno, M.; Tributsch, H. Over 18% Solar Energy Conversion to Generation of Hydrogen Fuel; Theory and Experiment for Efficient Solar Water Splitting. *Int. J. Hydrogen Energy* **2001**, *26* (7), 653–659.

(18) Qiu, J.; Zeng, G.; Ha, M.-A.; Hou, B.; Mecklenburg, M.; Shi, H.; Alexandrova, A. N.;

Cronin, S. B. Microscopic Study of Atomic Layer Deposition of TiO_2 on GaAs and Its Photocatalytic Application. *Chem. Mater.* **2015**, *27* (23), 7977–7981.

(19) Hu, S.; Shaner, M. R.; Beardslee, J. a; Lichterman, M.; Brunschwig, B. S.; Lewis, N. S. Amorphous TiO_2 Coatings Stabilize Si, GaAs, and GaP Photoanodes for Efficient Water Oxidation. *Science* **2014**, *344* (6187), 1005–1009.

(20) Gunawan; Septina, W.; Ikeda, S.; Harada, T.; Minegishi, T.; Domen, K.; Matsumura, M. Platinum and Indium Sulfide-Modified CuInS 2 as Efficient Photocathodes for Photoelectrochemical Water Splitting. *Chem. Commun.* **2014**, *50* (64), 8941.

(21) Luo, J.; Tilley, S. D.; Steier, L.; Schreier, M.; Mayer, M. T.; Fan, H. J.; Gratzel, M. Solution Transformation of Cu2O into CuInS2 for Solar Water Splitting. *Nano Lett.* **2015**, *15* (2), 1395–1402.

(22) Wang, J.; Zhang, P.; Song, X.; Gao, L. Cu2ZnSnS4 Thin Films: Spin Coating Synthesis and Photoelectrochemistry. *RSC Adv.* **2014**, *4*, 21318.

(23) Ros, C.; Andreu, T.; Giraldo, S.; Izquierdo-Roca, V.; Saucedo, E.; Morante, J. R. Turning Earth Abundant Kesterite-Based Solar Cells into Efficient Protected Water Splitting Photocathodes. *ACS Appl. Mater. Interfaces* **2018**, *10*, 13425−13433.

(24) Ros, C.; Andreu, T.; Giraldo, S.; Sánchez, Y.; Morante, J. R. Conformal Chalcopyrite Based Photocathode for Solar Refinery Applications. *Sol. Energy Mater. Sol. Cells* **2016**, *158*, 184–188.

(25) Liu, R.; Zheng, Z.; Spurgeon, J.; Yang, X. Enhanced Photoelectrochemical Water-Splitting Performance of Semiconductors by Surface Passivation Layers. *Energy Environ. Sci.* **2014**, *7* (8), 2504–2517.

(26) Hu, S.; Lewis, N. S.; Ager, J. W.; Yang, J.; McKone, J. R.; Strandwitz, N. C. Thin-

Film Materials for the Protection of Semiconducting Photoelectrodes in Solar-Fuel Generators. *J. Phys. Chem. C* **2015**, *119* (43), 24201–24228.

(27) Lichterman, M. F.; Sun, K.; Hu, S.; Zhou, X.; McDowell, M. T.; Shaner, M. R.; Richter, M. H.; Crumlin, E. J.; Carim, A. I.; Saadi, F. H.; et al. Protection of Inorganic Semiconductors for Sustained, Efficient Photoelectrochemical Water Oxidation. *Catal. Today* **2016**, *262*, 11–23.

(28) Wang, T.; Luo, Z.; Li, C.; Gong, J. Controllable Fabrication of Nanostructured Materials for Photoelectrochemical Water Splitting via Atomic Layer Deposition. *Chem. Soc. Rev.* **2014**, *43* (22), 7469–7484.

(29) Mei, B.; Pedersen, T.; Malacrida, P.; Bae, D.; Frydendal, R.; Hansen, O.; Vesborg, P. C. K.; Seger, B.; Chorkendorff, I. Crystalline TiO 2 : A Generic and Effective Electron-Conducting Protection Layer for Photoanodes and -Cathodes. *J. Phys. Chem. C* **2015**, *119* (27), 15019–15027.

(30) Mei, B.; Seger, B.; Pedersen, T.; Malizia, M.; Hansen, O.; Chorkendorff, I.; Vesborg, P. C. K. Protection of p + -n-Si Photoanodes by Sputter-Deposited Ir/IrO x Thin Films. *J. Phys. Chem. Lett.* **2014**, *5* (11), 1948–1952.

(31) Ros, C.; Carretero, N. M.; David, J.; Arbiol, J.; Andreu, T.; Morante, J. R. Insight into the Degradation Mechanisms of Atomic Layer Deposited TiO2 as Photoanode Protective Layer. *ACS Appl. Mater. Interfaces* **2019**, *Just accep*.

(32) Peng, T. C.; Xiao, X. H.; Han, X. Y.; Zhou, X. D.; Wu, W.; Ren, F.; Jiang, C. Z. Characterization of DC Reactive Magnetron Sputtered NiO Films Using Spectroscopic Ellipsometry. *Appl. Surf. Sci.* **2011**, *257* (13), 5908–5912.

(33) Dette, C.; Hurst, M. R.; Deng, J.; Nellist, M. R.; Boettcher, S. W. Structural Evolution

of Metal (Oxy)Hydroxide Nanosheets during the Oxygen Evolution Reaction. **2018**.

(34) Jang, W. L.; Lu, Y. M.; Hwang, W. S.; Hsiung, T. L.; Wang, H. P. Point Defects in Sputtered NiO Films. *Appl. Phys. Lett.* **2009**, *94* (6), 92–95.

(35) D'Amario, L.; Boschloo, G.; Hagfeldt, A.; Hammarström, L. Tuning of Conductivity and Density of States of NiO Mesoporous Films Used in P-Type DSSCs. *J. Phys. Chem. C* **2014**, *118* (34), 19556–19564.

(36) Sato, H.; Minami, T.; Takata, S.; Yamada, T. Transparent Conducting P-Type NiO Thin Films Prepared by Magnetron Sputtering. *Thin Solid Films* **1993**, *236* (1–2), 27–31.

(37) Scheuermann, A. G.; McIntyre, P. C. Atomic Layer Deposited Corrosion Protection: A Path to Stable and Efficient Photoelectrochemical Cells. *J. Phys. Chem. Lett.* **2016**, *7* (14), 2867–2878.

(38) Miikkulainen, V.; Leskelä, M.; Ritala, M.; Puurunen, R. L.; Leskelä, M.; Ritala, M.; Puurunen, R. L. Crystallinity of Inorganic Films Grown by Atomic Layer Deposition: Overview and General Trends. *J. Appl. Phys.* **2013**, *113* (2), 021301.

(39) Flox, C.; Murcia-López, S.; Carretero, N. M.; Ros, C.; Morante, J. R.; Andreu, T. Role of Bismuth in the Electrokinetics of Silicon Photocathodes for Solar Rechargeable Vanadium Redox Flow Batteries. *ChemSusChem* **2017**, *08028*, 125–129.

(40) Lu, H. L.; Scarel, G.; Wiemer, C.; Perego, M.; Spiga, S.; Fanciulli, M.; Pavia, G. Atomic Layer Deposition of NiO Films on Si(100) Using Cyclopentadienyl-Type Compounds and Ozone as Precursors. *J. Electrochem. Soc.* **2008**, *155* (10), H807.

(41) Lindahl, E.; Ottosson, M.; Carlsson, J. O. Atomic Layer Deposition of NiO by the Ni(Thd)2/H2O Precursor Combination. *Chem. Vap. Depos.* **2009**, *15* (7–9), 186–191.

(42) Trotochaud, L.; Young, S. L.; Ranney, J. K.; Boettcher, S. W. Nickel-Iron Oxyhydroxide Oxygen-Evolution Electrocatalysts: The Role of Intentional and Incidental Iron Incorporation. *J. Am. Chem. Soc.* **2014**, *136* (18), 6744–6753.

(43) Nardi, K. L.; Yang, N.; Dickens, C. F.; Strickler, A. L.; Bent, S. F. Creating Highly Active Atomic Layer Deposited NiO Electrocatalysts for the Oxygen Evolution Reaction. *Adv. Energy Mater.* **2015**, *5* (17), 1–10.

(44) Hassan, A. J. Study of Optical and Electrical Properties of Nickel Oxide (NiO) Thin Films Deposited by Using a Spray Pyrolysis Technique. **2014**, No. December, 2184–2191.

(45) Sun, K.; Kuang, Y.; Verlage, E.; Brunschwig, B. S.; Tu, C. W.; Lewis, N. S. Sputtered NiOx Films for Stabilization of P+n-InP Photoanodes for Solar-Driven Water Oxidation. *Adv. Energy Mater.* **2015**, *5* (1402276), 1–8.

(46) Chen, H. L.; Yang, Y. S. Effect of Crystallographic Orientations on Electrical Properties of Sputter-Deposited Nickel Oxide Thin Films. *Thin Solid Films* **2008**, *516* (16), 5590–5596.

(47) Sun, K.; Saadi, F. H.; Lichterman, M. F.; Hale, W. G.; Wang, H.-P.; Zhou, X.; Plymale, N. T.; Omelchenko, S. T.; He, J.-H.; Papadantonakis, K. M.; et al. *Stable Solar-Driven Oxidation of Water by Semiconducting Photoanodes Protected by Transparent Catalytic Nickel Oxide Films*; 2015; Vol. 112.

(48) Jang, W.; Lu, Y.; Hwang, W.; Hsiung, T.; Wang, H. P. Surface & Coatings Technology Effect of Substrate Temperature on the Electrically Conductive Stability of Sputtered NiO Fi Lms. *Surf. Coat. Technol.* **2008**, *202* (22–23), 5444–5447.

(49) B.D. Cullity. *Elements of X-RAY DIFFRACTION Second Edition*; 1978.

(50) Scheuermann, A. G.; Kemp, K. W.; Tang, K.; Lu, D. Q.; Satterthwaite, P. F.; Ito, T.; Chidsey, C. E. D. D.; McIntyre, P. C.; Mc Intyre, P. C. Conductance and Capacitance of Bilayer Protective Oxides for Silicon Water Splitting Anodes. *Energy Environ. Sci.* **2016**, *9* (2), 1–26.

(51) Dueñas, S.; Castán, H.; García, H.; Andrés, E. S.; Toledano-Luque, M.; Mártil, I.; González-Díaz, G.; Kukli, K.; Uustare, T.; Aarik, J. A Comparative Study of the Electrical Properties of TiO 2 Films Grown by High-Pressure Reactive Sputtering and Atomic Layer Deposition. *Semicond. Sci. Technol.* **2005**, *20* (10), 1044–1051.

(52) Bachmann, J.; Zolotaryov, A.; Albrecht, O.; Goetze, S.; Berger, A.; Hesse, D.; Novikov, D.; Nielsch, K. Stoichiometry of Nickel Oxide Films Prepared by ALD. *Chem. Vap. Depos.* **2011**, *17* (7–9), 177–180.

(53) Niinistö, J.; Putkonen, M.; Niinistö, L.; Arstila, K.; Sajavaara, T.; Lu, J.; Kukli, K.; Ritala, M.; Leskelä, M. HfO[Sub 2] Films Grown by ALD Using Cyclopentadienyl-Type Precursors and H[Sub 2]O or O[Sub 3] as Oxygen Source. *J. Electrochem. Soc.* **2006**, *153* (3), F39.

(54) Fujii, T.; Arita, M.; Hamada, K.; Takahashi, Y.; Sakaguchi, N. In-Situ Transmission Electron Microscopy of Conductive Filaments in NiO Resistance Random Access Memory and Its Analysis. *J. Appl. Phys.* **2013**, *113* (8).

(55) Nardi, F.; Deleruyelle, D.; Spiga, S.; Muller, C.; Bouteille, B.; Ielmini, D. Switching of Nanosized Filaments in NiO by Conductive Atomic Force Microscopy. *J. Appl. Phys.* **2012**, *112* (6).

(56) Nachman, M.; Cojocaru, L. N.; Rîbco, L. V. Electrical Properties of Non-Stoichiometric Nickel Oxide. *Phys. Status Solidi* **1965**, *8* (3), 773–783.

(57) Jiang, F.; Choy, W. C. H.; Li, X.; Zhang, D.; Cheng, J. Post-Treatment-Free Solution-Processed Non-Stoichiometric NiOx Nanoparticles for Efficient Hole-Transport Layers of Organic Optoelectronic Devices. *Adv. Mater.* **2015**, *27* (18), 2930–2937.

(58) Kuanr, S. K.; Vinothkumar, G.; Babu, K. S. Substrate Temperature Dependent Structural Orientation of EBPVD Deposited NiO Films and Its Influence on Optical, Electrical Property. *Mater. Sci. Semicond. Process.* **2018**, *75* (November 2017), 26–30.

(59) Bae, D.; Seger, B.; Vesborg, P. C. K.; Hansen, O.; Chorkendorff, I. Strategies for Stable Water Splitting via Protected Photoelectrodes. *Chem. Soc. Rev.* **2017**, *46* (7), 1933–1954.

(60) Hamann, T. W. Water Splitting: An Adaptive Junction. *Nat. Mater.* **2014**, *13* (1), 3–4.

(61) Digdaya, I. A.; Adhyaksa, G. W. P.; Trzesniewski, B. J.; Garnett, E. C.; Smith, W. A. Interfacial Engineering of Metal-Insulator-Semiconductor Junctions for Efficient and Stable Photoelectrochemical Water Oxidation. *Nat. Commun.* **2017**, *8* (May), 15968.

(62) Mills, T. J.; Lin, F.; Boettcher, S. W. Theory and Simulations of Electrocatalyst-Coated Semiconductor Electrodes for Solar Water Splitting. *Phys. Rev. Lett.* **2014**, *112* (14), 1–5.

(63) Lin, F.; Boettcher, S. W. Adaptive Semiconductor/Electrocatalyst Junctions in Water-Splitting Photoanodes. *Nat. Mater.* **2014**, *13* (1), 81–86.

(64) Lin, F.; Bachman, B. F.; Boettcher, S. W. Impact of Electrocatalyst Activity and Ion Permeability on Water-Splitting Photoanodes. *J. Phys. Chem. Lett.* **2015**, *6* (13), 2427–2433.

(65) Samin, A. J.; Taylor, C. D. An Analysis of Limiting Cases for the Metal Oxide Film Growth Kinetics Using an Oxygen Defects Model Accounting for Transport and

Interfacial Reactions. **2018**, *43* (4), 317–326.

(66) Sharel, P. E.; Liu, D.; Lazenby, R. A.; Sloan, J.; Vidotti, M.; Unwin, P. R.; Macpherson, J. V. Electrodeposition of Nickel Hydroxide Nanoparticles on Carbon Nanotube Electrodes: Correlation of Particle Crystallography with Electrocatalytic Properties. *J. Phys. Chem. C* **2016**, *120* (29), 16059–16068.

(67) Wang, X.; Wang, Y.; Zhao, C.; Zhao, Y.; Yan, B.; Zheng, W. Electrodeposited Ni(OH)2 Nanoflakes on Graphite Nanosheets Prepared by Plasma-Enhanced Chemical Vapor Deposition for Supercapacitor Electrode. *New J. Chem.* **2012**, *36* (9), 1902–1906.

(68) Hall, D. S.; Lockwood, D. J.; Bock, C.; MacDougall, B. R. Nickel Hydroxides and Related Materials: A Review of Their Structures, Synthesis and Properties. *Proc. R. Soc. A Math. Phys. Eng. Sci.* **2015**, *471* (2174).

(69) Huang, L. F.; Hutchison, M. J.; Santucci, R. J.; Scully, J. R.; Rondinelli, J. M. Improved Electrochemical Phase Diagrams from Theory and Experiment: The Ni-Water System and Its Complex Compounds. *J. Phys. Chem. C* **2017**, *121* (18), 9782–9789.

TOC

The degradation mechanisms of ALD-grown NiO protective layers over 1000 h at anodic alkaline conditions are identified and a recovery mechanism is presented